

Analytical and multicoupled methods for optimal steady-state thermoelectric solutions

Pablo Moreno-Navarro^{*1}, José L. Pérez-Aparicio^{1a} and J.J. Gómez-Hernández^{2b}

¹Department of Continuum Mechanics & Theory of Structures, Universitat Politècnica de València, Camino de Vera, s/n, Valencia 46022, Spain

²Research Institute of Water and Environmental Engineering, Universitat Politècnica de València, Camino de Vera, s/n, Valencia 46022, Spain

(Received January 3, 2022, Revised February 8, 2022, Accepted February 10, 2022)

Abstract. Peltier cells have low efficiency, but they are becoming attractive alternatives for affordable and environmentally clean cooling. In this line, the current article develops closed-form and semianalytical solutions to improve the temperature distribution of Bi_2Te_3 thermoelements. From the distribution, the main objective of the current work—the optimal electric intensity to maximize cooling—is inferred. The general one-dimensional differential coupled equation is integrated for linear and quadratic geometry of thermoelements, under temperature constant properties. For a general shape, a piece-wise solution based on heat flux continuity among virtual layers gives accurate analytical solutions. For variable properties, another piece-wise solution is developed but solved iteratively. Taking advantage of the formulae, the optimal intensity is directly derived with a minimal computational cost; its value will be of utility for more advanced designs. Finally, a parametric study including straight, two linear, barrel, hourglass and vase geometries is presented, drawing conclusions on how the shape of the thermoelement affects the coupled phenomena. A specially developed coupled and non-linear finite element research code is run taking into account all the materials of the cell and using symmetries and repetitions. These accurate results are used to validate the analytical ones.

Keywords: analytical solution; multiphysics; non-linear finite element; optimal intensity; thermoelectric; thermoelement shape

1. Introduction

Peltier cells based on TM are used for the cooling of many devices. The general advantages of these cells are their simplicity of construction and assembly, their solid state nature along with the capability of being miniaturized, but the main disadvantage is their very low performance. New materials based on metallic oxides or nanotechnology could almost double this performance although it is doubtful that in the medium term it could surpass 15%. The classical reference Rowe (2018) already stated that the optimal TE length is between 1×10^{-3} and 2×10^{-3} [m] but did not elaborate on the shape of the TE.

*Corresponding author, Ph.D., E-mail: pabmona@upv.es

^aProfessor, E-mail: jopeap@mes.upv.es

^bProfessor, E-mail: jgomez@upv.es

From the start of their development and application, constant square cross-section (parallelepipeds) TE have been assembled, probably due to their facility of manufacturing. Currently and with the arrival of new techniques in nano-and meso-machining technologies and even additive manufacturing with 3D printing Mallick *et al.* (2020), virtually any geometry can be produced at a reasonable price. The objective of the current work is to investigate TE geometries that in the future could improve the performance of *Peltier* cells.

To this end, closed-form and semi-analytical formulae are developed here not only for simple shapes but to completely general ones, with the future aim of automatically optimize them, even in dynamic situations, for different objectives. To verify the validity of the solutions, a complete non-linear FE algorithm developed in previous publications, Moreno-Navarro *et al.* (2018), Pérez-Aparicio *et al.* (2016b), Palma *et al.* (2012) and Palma *et al.* (2013) is run. This FE can model transient states, fully and dynamically couples the thermal, electric, and elastic fields, can account for T -dependent properties and has been implemented in the research code FEAP, Taylor (2010).

Several publications have already demonstrated the importance of the TE geometry, Dongxua *et al.* (2019), Lamba *et al.* (2018). The first optimized parallelepipedal TE modules in TEG mode. The objectives included the number of TC in a module and the optimal TE height, calculated with an iterative model and validated with experiments. The second, also optimized TEG with a genetic algorithm but only for a trapezoidal TE. The parameters were the TE height, electric current, cold and hot faces T ratio and cooling capacity. An analytical model based on thermodynamic principles was applied, the material properties were dependent on T and the *Thomson* effect was considered.

Also, it already has been demonstrated that optimal TE lengths and linear variations in the vertical direction (between the hot and cold faces) can improve the TE efficiency with respect to the standard geometry, especially in transient situations. On this line, Lv *et al.* (2016) applied a numerical model (not based on FE) for the optimization of TE. To determine optimal steady-state electric intensity values, the model found minimums from several cases. With a parametric study, conclusions on best linear geometries were drawn.

A simple static TE electric generator with linear variation of A was optimized in Sahin and Yilbas (2013); they presented analytical formulae for the optimal steady-state I_{op} . The algorithm was again conjugate-gradient based. Two single-objective optimizations, one for thermal efficiency and another for electric power, and a multiobjective for both together was addressed. The publication concluded that higher TE slopes (regardless of the sign) lead to better efficiency but worse extracted power.

In the thorough Lin and Yu (2016), a *Peltier* cell with three parts in the same TC (top part with constant section, lower part with two p- and n-doped linearly increasing sections) was studied with an analytical model that partially included T -dependent properties. The total l , cold face A and T_c were fixed for static conditions. But the average T was variable, affecting the COP and Q_{css} . Optimization algorithms were not applied but, through a parametric study, it was demonstrated that the variation of the lower part was beneficial, although their relative lengths with respect to the top straight element needed to be quantified for each application.

The reference Fabián-Mijangos *et al.* (2017) emphasized that the geometry of the TE legs is fundamental to improve the performance of TEG. Studies with an analytical model for trapezoidal TE and comparisons with proof-of concept devices showed that figure of merit could be doubled. Recently, Siddique *et al.* (2020) presented a study in which TE materials were manufactured in straight and linear shapes, including microstructural characterization. Comparisons of results of a simplified analytical model and of experiments were used to generate curves and find optimal electric intensities, with some discrepancies due to uncertainties of the measuring instruments and

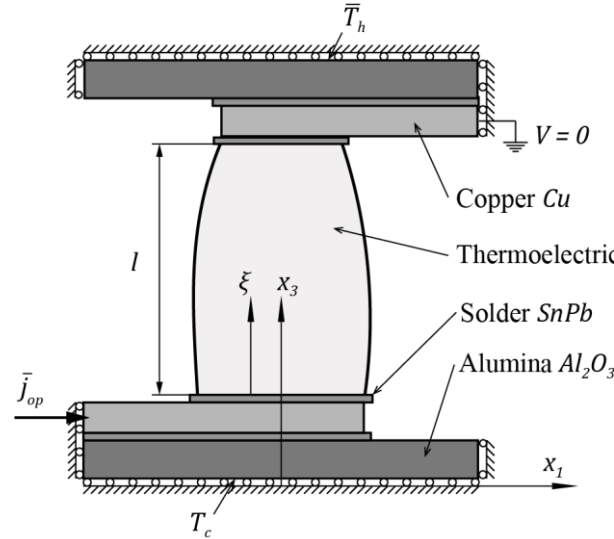


Fig. 1 Scheme of a half-thermocouple with boundary conditions: mechanically hinged at hot and cold faces, repetition at left and symmetry at right; thermoelement geometry has variable area. Prescribed magnitudes noted by an overbar

incompleteness of the model. It was stated that if the cold face has smaller area than the hot face, the maximum heat power drawn is obtained with less intensity and vice versa.

Finally, Wang *et al.* (2021) thoroughly studied the performance of static TEG with a simple diffusion-convection analytical model but incorporating in the differential equation a quadratic varying TE area. The model was validated with a commercial FE code and several optimal shapes obtained. Their main conclusion is that changes of the TE shape do not improve the obtained voltage, coinciding with the present paper.

2. Materials and method

For the heat pump application studied in the present work, it is assumed that the electric flux j is conserved and that all distributions of T, V , fluxes, stresses, etc. are equal inside each of the two TE, except for a sign change of some distributions. Therefore, two vertical planes of symmetry and one of repetition at the left can be considered and only one quarter of the TC has to be modeled with the proper mechanical BC (see Fig. 1). Of the different mechanical BC which can be prescribed in the hot and cold faces, hinged surfaces are chosen. The heat convection loss from any solid-air interface is neglected and the electric and thermal contact surfaces are considered perfect. The *Thomson* effect is also neglected in analytical developments, but it is included in the FE runs with T -dependencies of the material properties.

The electric field is gauged to zero with $\bar{V} = 0$ [V], \bar{T}_h is set to 50 [°C] and the steady-state optimal \bar{J}_{op} is prescribed using a special interface FE developed in Pérez-Aparicio *et al.* (2012). The thermal flux is forced nil in the cold face, $Q_c = 0$ [W], providing an adiabatic BC. Although the temperatures will be reported in *Celsius* degrees, the analytical formulation of Section 3 is developed in *Kelvin* degrees.

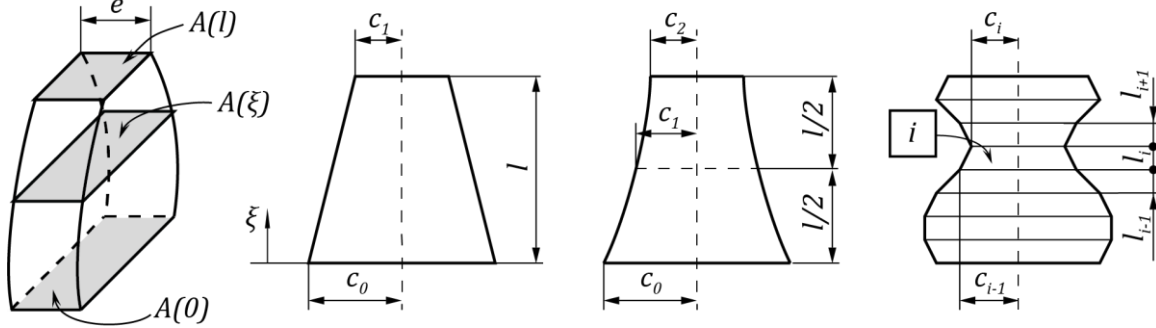


Fig. 2 Vertical thermoelement geometries. From left to right: three-dimensional view, linear, quadratic, piecewise linear (divided into layers i)

Table 1 Properties of the *Peltier* cell materials from Fig. 1. Temperature-dependent properties for Bi_2Te_3 given in Eq. (1)

Property.	Unit	Al_2O_3	Cu	$SnPb$	Bi_2Te_3
κ	[W/K·m]	35.3	386	48	Eq. (1)
$\gamma \times 10^6$	[A/V·m]	0	58.1	4.72	Eq. (1)
α	[V/K]	0	0	0	Eq. (1)

The thickness e in the x_2 direction (see Fig. 2) is constant, a condition that could easily be overcome but facilitates the construction of the FE mesh for the non-TE parts and specially the definition of the analytical model.

In Section 3 and for any TE shape, the main objective of the current work is to find the intensity I_{op} so that a minimum T_{CSS} -temperature of the cold face at steady-state can be reached. Optimal intensities have been obtained in the past but in general for parallelepipedal (straight) or linear TE, viz. Rowe (2018) or Pérez-Aparicio *et al.* (2016a).

First, compact analytical expressions are calculated for linear and quadratic TE shapes assuming material properties that do not change with T : this hypothesis is called “constant properties” or CP. Second, general geometries are considered by piecewise superposition of virtual linear layers with the necessary continuity and another compact analytical expression is provided under CP. Finally, an iterative procedure is described under VP since the real TE material properties are in general T -dependent.

A complete parametric study of five predetermined geometries with different l is presented in Section 4, under a step pulse and both for steady and transient states.

The material properties used throughout the calculations are listed in Table 1 and Eq. (1), the latter interpolated from the curves of Rowe (2018).

$$\begin{aligned}
 \alpha(T) &= 1.988 \times 10^{-4} + 3.353 \times 10^{-7} T + 7.52 \times 10^{-10} T^2 \\
 \kappa(T) &= 1.663 - 3.58 \times 10^{-3} T + 3.195 \times 10^{-5} T^2 \\
 \gamma(T) &= 1.096 \times 10^5 - 5.59 \times 10^2 T + 2.498 T^2
 \end{aligned} \tag{1}$$

The hypotheses assumed in the current models can be listed as:

- All variables can only be a function of ξ , i.e., they are equal in the transversal planes.
- Material properties of each layer are not T -dependent and they are calculated with the average

T of both ends.

- The thickness of the TE is constant (dimension e).
- Convection and radiation of the lateral faces is assumed to be negligible.
- For the multilayer cases, the geometrical variation is linear and for VP the equations' solution are iterative.

3. Optimal intensity for variable sections

When general geometries are considered, the steady-state optimal I_{op} can significantly differ from that of a straight TE. In this section, new equations are developed for an arbitrary geometry expanding the simple solution given in Pérez-Aparicio *et al.* (2016a). The 1D power balance equation of this reference is rewritten since now the equilibrium of heat energy is completely cross-sectional dependent. Neglecting the *Thomson* effect

$$\frac{1}{A(\xi)} \frac{d}{d\xi} \left[\kappa(T) A(\xi) \frac{dT}{d\xi} \right] + \frac{I^2}{A^2(\xi) \gamma(T)} = 0 \quad (2)$$

where A is a function of the vertical TE-local coordinate ξ (see Fig. 2). To preserve electric charge, it will be assumed that I is constant, that is, $j_3 = I/A$ is variable with ξ . Both κ and γ are in general T -dependent (see Eq. (1)), although for simplicity in the ensuing three subsections the properties are considered CP. The variable $A(\xi)$ is assumed rectangular, see the first Fig. 1.

The first term in the equation represents thermal conduction; the second is the generated *Joule* source of heat per unit of volume. The *Peltier* effect will be introduced through the following transport Eq. (5).

3.1 Linear geometry, constant properties

The linear geometry is represented in the second of Fig. 2, with a linear variation of $A(\xi)$ in the frontal plane $x_1 x_3$ given by

$$A(\xi) := d_0 + d_1 \xi = 2e \left[c_0 + (c_1 - c_0) \frac{\xi}{l} \right] \quad (3)$$

where c_0 and c_1 are the half-widths at the bottom and top sections respectively, d_0 the area at $\xi = 0$ and d_1 its slope. Using this expression in Eq. (2), the T distribution can be solved as a function of the a-priori unknown BC $T(0) \approx T_c$ and of the prescribed $T(l) \approx \bar{T}_h$. This is the first approximation assumed by the 1D model, assigning to the two TE ends the real cold and hot faces, which in reality should be the two Al_2O_3 external surfaces; the approximation is valid since the thermal conductivity of solder, copper and alumina are high (see Table 1). By direct integration

$$T(\xi) = \frac{\phi_{0\xi} \bar{T}_h + \phi_{\xi l} T_c}{\phi_{0l}} + \frac{I^2}{2\gamma\kappa} \phi_{0\xi} \phi_{\xi l}; \quad \phi_{ab} = \frac{1}{d_1} \ln \frac{A(a)}{A(b)} \quad (4)$$

where subindexes a, b can take the values $0, \xi$ or l . The form factor ϕ contains the information of the geometry; as in the following subsections for other contours, this factor is undetermined when the section becomes constant. Taking the limit when $d_1 \rightarrow 0$, the result $\phi_{ab} = (a - b)/d_0$ is obtained and by using this term in Eq. (4) we recover the expression from Pérez-Aparicio *et al.*

(2016a) for constant section $\phi_{0l} = -l/A$.

In a 1D model, the heat power can be expressed at steady-state under CP by the differential expression (viz. Rowe (2018))

$$Q(\xi) = \alpha IT(\xi) - \kappa A(\xi) \frac{dT(\xi)}{d\xi} \quad (5)$$

To calculate the CP from Eq. (1), an assumed average $T_{av} = 10$ [°C] is considered in the material properties of the polynomials. The Eq. (5) is evaluated on the cold face $Q_c := Q(0)$ and then the intensity that maximizes the increment of T is found by solving $dQ_c/dI = 0$

$$I_{op} = -\frac{\alpha \gamma T_{css}}{\phi_{0l}} \quad (6)$$

The previous expression depends on the unknown T_{css} , the value for which no additional heat power can be taken from the cold face. Under this temperature Q_c must be zero, or equivalently $\bar{T}_h - T_c$ is maximized at steady-state. Imposing $Q_c = 0$ in Eq. (5) and replacing the derivative of $T(\xi)$ from Eq. (4)

$$T_{css} = \frac{-\kappa + \sqrt{\kappa^2 + 2\bar{T}_h \alpha^2 \gamma \kappa}}{\alpha^2 \gamma} \quad (7)$$

This equation depends only on the known \bar{T}_h and on material properties, and it is exactly the same one as that obtained for a constant section in Pérez-Aparicio *et al.* (2016a), verifying that T_{css} does not depend on the TE linear geometry under CP. The final optimal intensity is obtained substituting Eq. (7) into Eq. (6).

3.2 Quadratic geometry, constant properties

The quadratic geometry is shown in the third of Fig. 2. Three parameters are used to specify the variation of $A(\xi)$: the TE half-widths at the bottom, middle and top

$$A(\xi) := d_0 + d_1 \xi + d_2 \xi^2 = 2e \left[c_0 - (3c_0 - 4c_1 + c_2) \frac{\xi}{l} + 2(c_0 - 2c_1 + c_2) \left(\frac{\xi}{l} \right)^2 \right] \quad (8)$$

Following the same procedure as in the previous subsection but with the previous quadratic area, the resulting expression for T is the same as that of Eq. (4) left but with the form factors

$$\phi_{ab} = 2 \frac{\mathcal{A}_b - \mathcal{A}_a}{\Delta}; \quad \mathcal{A}_a = \arctg \left(\frac{1}{\Delta} \frac{dA}{d\xi}(a) \right); \quad \Delta = \sqrt{4d_0 d_2 - (d_1)^2} \quad (9)$$

where \mathcal{A}_b would be defined by the middle expression but particularized in b . Note that Δ can be pure imaginary, but then the numerator of the first of Eqs. (9) would also be pure imaginary due to the arctg function and then the quotient results in a real number. If $d_1 = d_2 = 0$ (constant section) or $d_2 = 0$ (linear section), the Eq. (9) is indeterminate. But it can be shown that in the limit as $d_2 \rightarrow 0$, the result tends to that of Eq. (4); likewise, in the limit when both $d_1, d_2 \rightarrow 0$, the result coincides with that of a constant section.

Repeating the steps from the previous subsection for I_{op} , we again obtain the Eq. (7) and in addition I_{op} is given by the Eq. (6) but with the quadratic ϕ_{ab} from Eq. (9).

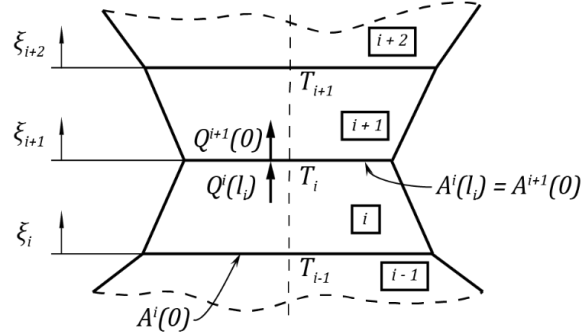


Fig. 3 Detailed view of the piecewise linearized geometry of the right Fig. 2; each layer includes local coordinates. Continuity of heat power at interfaces must be imposed

3.3 General geometry, constant properties

For complex geometries, an extension of the previous approaches becomes very cumbersome. Instead of working out results based on higher order polynomials or other analytical functions, the previous findings can be applied to a piecewise-linear geometry.

The length of the TE is divided into n “layers”, each with linear lateral sides of variable area $A^i(\xi_i) = d_0^i + d_1^i \xi_i$. This linear variation could be changed to a quadratic one but not much difference would be obtained if the layers are thin with respect to l . The lengths l_i do not need to be equal but are subjected to the constraint $\sum_1^n l_i = l$ (right of Fig. 2).

For each layer $1 \leq i \leq n$, a local vertical coordinate $0 \leq \xi_i \leq l_i$ is defined as shown in Fig. 3. The temperature and the half-width at the top interface of each layer are denoted by T_i and c_i . At the bottom interface, the two are named T_{i-1} and c_{i-1} , so that for the first layer $T^1(0) := T_0 \approx T_c$ and for the last $T^n(l_n) := T_n \approx \bar{T}_h$ (superscripts indicate the corresponding layer). The developments for a generic layer are conceptually similar to those of Section 3.1 of a completely linear TE, but now the layer solution $T^i(\xi_i)$ depends on the a-priori unknowns BC $T^i(0) := T_{i-1}$ and $T^i(l_i) := T_i$ instead of on \bar{T}_h and T_c .

Next, Eq. (2) is solved for the $T^i(\xi_i)$ distribution inside each layer-and therefore for the whole TE-resulting in a closed-form expression similar to Eq. (4)

$$T^i(\xi_i) = \frac{\phi_{0\xi_i} T_i + \phi_{\xi_i l_i} T_{i-1}}{\phi_{0l_i}} + \frac{I^2}{2\gamma\kappa} \phi_{0\xi_i} \phi_{\xi_i l_i} \quad (10)$$

The T -field is continuous by construction and so is I by conservation of charge. The solution on the layer interfaces is then obtained by enforcing the remaining continuity of heat power

$$Q^i(l_i) = Q^{i+1}(0); \quad i = 1, \dots, n-1 \quad (11)$$

the values of which from Eq. (5) are

$$\begin{cases} Q^i(l_i) = \alpha I T_i - \kappa A^i(l_i) \left. \frac{dT^i(\xi_i)}{d\xi_i} \right|_{\xi_i=l_i} \\ Q^{i+1}(0) = \alpha I T_i - \kappa A^{i+1}(0) \left. \frac{dT^{i+1}(\xi_{i+1})}{d\xi_{i+1}} \right|_{\xi_{i+1}=0} \end{cases} \quad (12)$$

Since by definition $A^i(l_i) := A^{i+1}(0)$, the continuity directly applies to the first derivatives of T . Eqs. (11) and (12) conform a system of $n - 1$ equations each one with four unknowns: T_{i-1}, T_i, T_{i+1} (see Eq. (10)) plus I . This system is not explicitly solvable since it has not been fully demonstrated that T_c can be calculated from Eq. (7) and a good estimate for I is not yet available. But starting from the top layer n and through substitution of one layer after the other, the generic interface T_i can be solved as an independent function of only the two unknowns T_c and I

$$T_i = \frac{\bar{T}_h \sum_{j=1}^i \phi_j + T_c \sum_{j=i+1}^n \phi_j}{\sum_{j=1}^n \phi_j} + \frac{I^2}{2\gamma\kappa} \sum_{j=1}^i \phi_j \sum_{j=i+1}^n \phi_j \quad (13)$$

where ϕ_j (short for $\phi_{0l|j}$) denotes in local coordinates the form factor between the top and bottom interfaces of layers $1 \leq j \leq n$.

As before, Q_c is obtained evaluating Eq. (12) at the cold face (first layer $i = 1$), but now as a function of T_1 (to be determined from Eq. (13)) instead of \bar{T}_h . The resulting heat power as function of the two main unknowns is

$$Q_c = \frac{I^2}{2\gamma} \sum_i^n \phi_i + \alpha I T_c + \kappa \frac{\bar{T}_h - T_c}{\sum_i^n \phi_i} \quad (14)$$

Analyzing the Eq. (14), it is interesting to note that the contribution to Q_c of the *Joule* effect (first term, right hand side) is always negative (descending the TE against ξ) since ϕ_i is also always negative; the contribution of heat conduction (third term) is also negative. The contribution of *Peltier* (middle term) is always positive (ascending) and does not depend on the geometry.

With the previous expression, and applying a maximization approach similar to the one described in Section 3.1, we obtain the compact equation

$$I_{op} = - \frac{\alpha \gamma T_{css}}{\sum_i^n \phi_i} \quad (15)$$

where only the denominator changes with respect to Eq. (6). It can be shown that the linear geometry of Eq. (6), is recovered from Eq. (15) by taking the limit of the equation for ϕ_i so that a continuous linear geometry is represented.

The maximum heat taken from the cold side at steady-state is determined by replacing Eq. (15) into Eq. (14)

$$Q_{css} = \frac{2\kappa(\bar{T}_h - T_{css}) - \alpha^2 \gamma T_{css}^2}{2 \sum_i^n \phi_i} \quad (16)$$

If the BC $Q_c = 0$ is applied to Eq. (16), we recover Eq. (7), finally demonstrating that T_{css} does not depend on the geometry of the TE under CP and disambiguating Eq. (15).

4. General geometry, variable properties

To find completely general solutions, VP must be considered and therefore an iterative method based on CP layers is proposed. Analogously to the previous subsection, T_i can be calculated solving Eq. (2) for $T^i(\xi_i)$ using the adjacent unknown temperatures as BC; then the flux continuity of Eq. (11) is again applied. The counterpart of Eq. (13) is obtained as

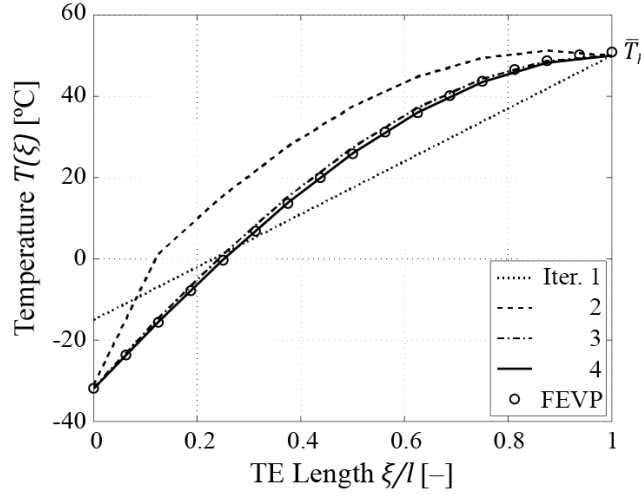


Fig. 4 Steady-state temperature distributions along a thermoelement for geometry **E** from Fig. 5. Four iterations of the semi-analytical solution based on Eq. (18) (lines) and finite element under variable properties (circles)

$$T_i = \frac{I^2 \left(\frac{\phi_i}{\gamma_i} + \frac{\phi_{i+1}}{\gamma_{i+1}} \right) + T_{i-1} \frac{\kappa_i}{\phi_i} + T_{i+1} \frac{\kappa_{i+1}}{\phi_{i+1}}}{I(\alpha_i - \alpha_{i+1}) + \frac{\kappa_i}{\phi_i} + \frac{\kappa_{i+1}}{\phi_{i+1}}} \quad (17)$$

valid for each $1 \leq i \leq n-1$ and function of $\alpha_i = \alpha(T_{av}|_i)$ to be calculated with the a priori unknown layer average $T_{av}|_i = (T_{i-1} + T_i)/2$ substituted in Eq. (1); the same dependency holds for κ_i and γ_i . Due to this additional implicitness, an iterative method must be applied. First, the Eq. (17) is particularized to the top interface of the bottom layer to calculate T_1 ; the unknowns of the right-hand side are now the material properties of layers $i = 1, 2$, besides T_c, T_2 and I . Subsequent particularizations to the other layers give $n-1$ implicit equations. Rearranging this system, T -expressions dependent now on the unknowns T_c, I plus the properties of all layers are given by the following functions f

$$\begin{aligned} T_1 &= f_1(T_c, \bar{T}_h, I, \alpha_1, \kappa_1, \gamma_1, \dots, \alpha_n, \kappa_n, \gamma_n) \\ T_2 &= f_2(T_c, \bar{T}_h, I, \alpha_1, \kappa_1, \gamma_1, \dots, \alpha_n, \kappa_n, \gamma_n) \\ &\vdots \\ T_{n-1} &= f_{n-1}(T_c, \bar{T}_h, I, \alpha_1, \kappa_1, \gamma_1, \dots, \alpha_n, \kappa_n, \gamma_n) \end{aligned} \quad (18)$$

The f explicit forms are too long to be written even for a few layers and they cannot directly be solved since an expression for T_c such as Eq. (7) cannot be explicitly found under VP.

The next step is to apply Eq. (5) to the bottom of the first layer

$$Q_c = -\frac{I^2}{2\gamma_1} \phi_1 + \alpha_1 I T_c - \kappa_1 \frac{T_1 - T_c}{\phi_1} \quad (19)$$

In this formula, the influence of the complete TE is in T_1 , to be substituted by the first of Eq. (18).

The maximization of Q_c to calculate I_{op} (similar to Eq. (6)) adds one equation. Finally, $Q_c =$

0 considering this I_{op} (similar to Eq. (14)) solves for T_{css} , but since these two equations cannot be derived in a closed form, a numerical approximation based on iterations is necessary.

The procedure is general, but as an example the process is presented for geometry **E** (defined in the next section) with just eight layers. First T_c is guessed as an arbitrary -15 [°C] and $T(\xi)$ linearly interpolated between this value and \bar{T}_h (straight dotted line in Fig. 4). With the resulting set of $T_{av}|_i$, the first iteration for the material properties is calculated for Eq. (18); the first additional equation gives I_{op} and the second T_{css} . With all T at the interfaces, the non-linear curve for the second iteration can be drawn. In this iteration the distribution does not have continuity of derivative at the first interface ($\xi = 0.125$), but in the third iteration the continuity is already completely fulfilled.

When I_{op} and/or T_{css} converge (usually with only three-four iterations) the final T distribution and the I_{op} value are found. Notice that although the first estimate of T_c is not close to the final value of -32 [°C], just in the second iteration an accurate value is obtained.

For further validation, the T distribution (considered “exact”) from the steady-state FEVP is plotted in the figure, achieving the semi-analytical model a very good agreement with it. The coincidence implies that the splitting of the general geometry into eight CP layers is accurate enough.

At any rate, the main interest of the analytical developments of this section is not to find T distributions but to rapidly obtain precise values of I_{op} for the FE runs, saving CPU resources for the time-consuming processes of transient behavior, optimization of geometry, pulse etc.

5. Parametric study

Six representative geometries shown of Fig. 5, each one divided into only eight equally spaced layers are studied in this section. There are no reasonable restrictions on the geometries to handle, although to avoid singular shapes, minimum and maximum widths are imposed. Geometry **S** is the traditional and the linear **A** and **B** the commonly studied in the literature of the last years (viz. Sahin and Yilbas (2013)). The rest are quadratic (**C**, **D**) and cubic (**E**). By construction and for comparison purposes, the smallest cross-section is half the width 1.5×10^{-3} [m] of the largest one for the first five geometries; therefore, in **D** the cold face is necessarily larger than that of **E** since its maximum is right above the cold face. The constant width of **S** is $2c = 1.125 \times 10^{-3}$ [m], an average of the maximum and minimum.

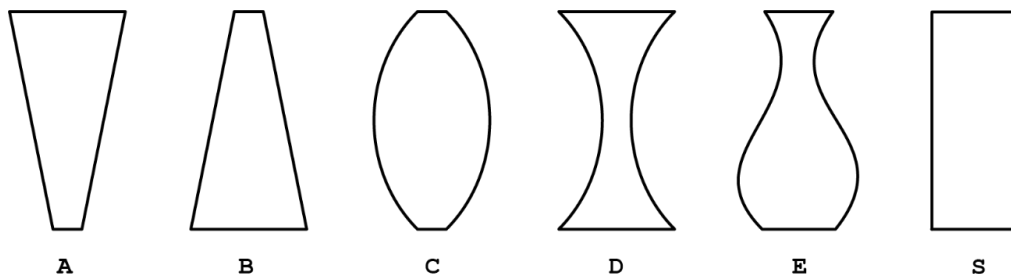


Fig. 5 Thermo-element geometries for parametric study: linear “pyramids” **A** and **B**, quadratic “barrel” **C** and “hourglass” **D**, cubic “vase” **E**, constant “straight” **S**. Cold face at bottom, hot face at top and equal maximum and minimum widths for all variable sections

Table 2 Optimal intensities to maximize overcooling at steady-state for thermoelement geometries of Fig. 5 (except **S**) with different lengths. Constant material properties and Finite Elements (FECP) and analytical (Anlt. CP) from Section 3.3 with eight layers

Geom.	$l \times 10^{-3}$ [m]	FECP		Anlt. CP	
		T_{css} [°C]	I_{op} [A]	T_{css} [°C]	I_{op} [A]
		A	4	-28.41	1.39
B	3	-28.06	1.84	-29.04	1.88
C	7	-28.55	0.88	-29.04	0.89
D	5	-28.62	0.99	-29.04	1.00
E	6	-28.61	0.92	-29.04	0.93

To present a broad sample and to investigate the dependency of I_{op} with the geometry, for all calculations the TE lengths are randomly assigned from the integer set $l \in \{3,4,5,6,7\} \times 10^{-3}$ [m] as listed in the next two tables.

Table 2 shows values of T_{css} calculated from Eq. (7) and numerically with the FECP. The Table also shows the optimal intensities calculated from Eq. (15) and using the bisection method of the FECP described in Pérez-Aparicio *et al.* (2016a). This method is much more time consuming because implies guessing an initial value, running four-five times the code and interpolating.

The FECP solution is used as a reference since it includes several nonlinearities, full process coupling, dynamics and all the materials of Fig. 1. The analytical solution is relatively simple to apply, it is based on a 1D geometry and only simulates the TM. In spite of these simplifications, the maximum errors are very small while the CPU and process times are orders of magnitude higher for FE. The T_{css} values from the analytical solution are constant since Eq. (7) is independent of geometry and length at steady-state (in transient-state the situation is different). But the values from FECP are not exactly equal due to the FE 3D discretization, which captures direction changes of fluxes from x_3 to x_2 and x_3 in the union between TE and Cu and in changes of $A(\xi)$: the shorter the TE the more important these 3D effects are.

In any case, the variable geometries and lengths have a small influence of only 3.4% and 2% for T_{css} and I_{op} respectively, partially validating the method of Section 3.3. As demonstrated in the previous section, I_{op} is not simply proportional to the inverse of l (as was the case for straight TE), but now to the inverse of the form factors.

Table 3 shows the same results as those of Table 2 but now under the VP hypothesis and using the semi-analytical method described in Section 3.4. The most important change between the two tables is a difference of 4% for I_{op} in geometry **B** and consequently 1.5% for T_{css} (in Kelvin scale). These differences are due to the inclusion of the Thomson effect $d\alpha/dT$ in the FEM formulation and in general to the completeness of its VP formulation. The variations among the T_{css} values for the different shapes are again small and similar to those of Table 2; for I_{op} they are even smaller.

All values of T_{css} are almost constant in spite of the geometry variation, for instance almost the same values are listed for **S** and **D** although with more electric consumption in the latter. But for transient-state studies (not developed in the current article), the advantages of some of the variable geometries will be significant.

Table 3 Optimal intensities to maximize overcooling at steady-state for geometries of Fig. 5; several lengths. Variable material properties and Finite Elements (FEVP) and semi-analytical (s-Anlt. VP) from Section 3.4 with eight layers

Geom.	$l \times 10^{-3}$ [m]	T_{css}		I_{op}	
		FECP		Anlt. CP	
		[°C]	[A]	[°C]	[A]
A	4	-31.86	1.45	-31.93	1.43
B	3	-31.51	1.92	-31.92	1.91
C	7	-32.01	0.91	-31.93	0.91
D	5	-32.07	1.03	-31.92	1.02
E	6	-32.05	0.95	-31.92	0.94
S	7	-32.12	0.77	-31.92	0.77

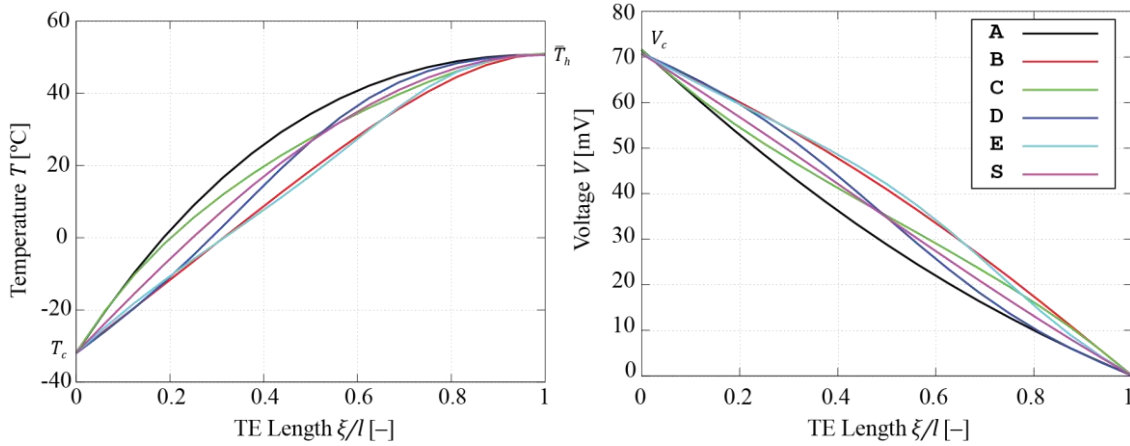


Fig. 6 Steady-state temperature distributions along the thermoelement center for the geometries of Fig. 5 using Finite Elements, variable material properties and the intensities of Table 3. Cold face $T_{css} \approx -32$ [°C] for all geometries with the same TE length of 5×10^{-3} [m]

The T distributions along the TE obtained with FEVP and under the different optimal intensities of Table 3 are plotted in Fig. 6 left. Note that the slope is highest (due to the *Joule* concentration) near the cold face for **A** and **C** with small cross-section on this face. For the same reason, the slope is highest in the middle of **D** and close to the hot face for **E**. This *Joule* concentration mostly determines the performance of each geometry as indicated by the last term of Eq. (2), inversely proportional to $A^2(\xi)$. Even if the equation is valid only in 1D, the electrical flow is mostly 1D and therefore the conclusion is valid for general symmetric geometries.

The T -values are substantially lower for **E** than for **A**, since the special geometry of the former is able to force a linear distribution up to the necking instead of a global quadratic for the latter: that is, for the same T values at both faces the vase shape reduces almost to half the *Joule* effect around the TE middle. The curvatures of the distributions at each position ξ/l are in general proportional to the geometrical widths, except close to the hot face where all temperatures must tend to the BC $\bar{T}_h = 50$ [°C]. The distribution of **S** is similar to that of **E**, but its T values are substantially higher in the middle.

These facts can also help to interpret the Eq. (5): as mentioned before its first term represents the *Peltier* effect function of $T(\xi)$, moving thermal energy from the cold to the hot face and the second term the *Fourier* effect function of $dT/d\xi$.

Near the hot face it can be appreciated that the slope of the distributions is almost horizontal, which means that the *Fourier* term must be very small since it is proportional to $dT/d\xi$; this nullity would not happen when the feeding electric intensity is smaller than I_{op} . On the other hand, near the cold face the BC $Q_c = 0$ implies that both terms must cancel each other, that is, the *Fourier* term and consequently the T -slope are different than zero.

In the right Fig. 6 the corresponding voltage distribution along the TE are plotted. The straight **S** shape produces an almost linear distribution, while **C** and **D** are non-linear but its values similar to those of **S**. The change of curvature of the last two is due to their symmetry with respect to the middle. The decreasing (with ξ) of the **E** and **B** distributions are very similar and maximize V at the center of the TE; the increasing a minimizes the voltage at the center for the contrary reason. In spite of their very different shapes, all geometries give a similar voltage at the cold face since its approximated expression is $V_{op} = \alpha \bar{T}_h$, independent of geometry.

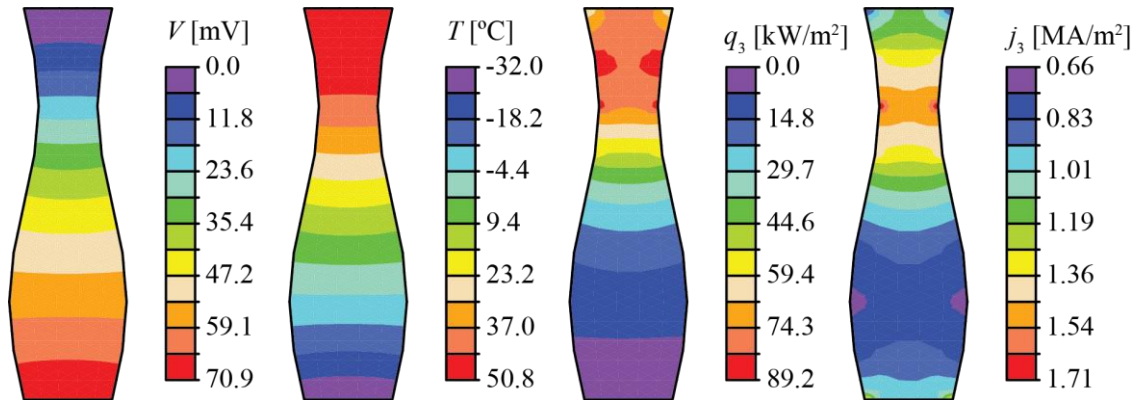


Fig. 7 Finite element distributions (under variable properties) for geometry **E** from Fig. 5 approximated with eight layers, along the vertical x_3 direction

In the Fig. 7 the 2D distributions obtained with FEVP are drawn; the refined mesh is built with 3D elements of 27 -nodes. Although as commented all materials of Fig. 1 are simulated, only the TE is shown. In the second left figure, the temperature is represented by almost horizontal isolines, giving validity to the second hypothesis assumed in Section 3. The spacing between color levels is constant in the first TE vertical half, and variable in the second in accordance with the distribution of the left Fig. 6. The voltage distribution of the left figure is also almost horizontal and equally-spaced except in the middle. The small departure from the horizontality is due to the variation of area.

For the two right figures the curvature of the isolines is much more evident, since the represented magnitude is the vertical component of the fluxes; both q_3 and j_3 are counterparts of Q and I per unit area; in any case, this curvature is so small that the unidimensionality is consider valid. The alterations in the necking are due to the non-zero horizontal component that reduces the module of the vertical component; that of the cold and specially the hot face to the change of direction of the

fluxes between the TM and copper, see the Fig. 1.

The hypotheses made in Section 3 can be verified in the Fig. 7: the isolines are almost horizontal implying constant T , and very similar values at the TE ends with respect to the real hot and cold faces: 51 vs. 50 top, -30.7 vs. -30.5 [°C] bottom.

6. Conclusions

In this article, compact analytical solutions are developed for the optimal intensity during steady-state of *Peltier* cells working as heat pumps, under the assumption of constant (with temperature) material properties and for general piecewise thermoelement geometries. For variable properties, an iterative semi-analytical method is presented and form factors for the new geometries are defined in all solutions.

The parametric study shows that at steady-state, the thermoelement geometry greatly affects the temperature distributions but not that of the cold face. The geometry also affects the *Joule* generation and the conduction but not the *Peltier* effect at steady-state. In future works it will be demonstrated that sophisticated geometries substantially affect the performance during the transient-state.

One of the interesting results is that for general geometries the optimal electric intensity is not proportional to the inverse of the thermoelement length (as for straight geometries) but to the inverse of trigonometric or logarithmic form factors dependent on the shape.

Acknowledgments

This work was supported by the Generalitat Valenciana research programmes PROMETEO/2020/016: Applications de Topologic Isolators in Spintronics and Thermoelectricity (TOP-TERM) and BEST/2021/079. The support is gratefully acknowledged.

References

- Dongxua, J., Zhongbaob, W., Pouc, J., Mazzonia, S., Rajood, S. and Romagnoli, A. (2019), "Geometry optimization of thermoelectric modules: Simulation and experimental study", *Energy Convers. Manage.*, **195**, 236-243. <https://doi.org/10.1016/j.enconman.2019.05.003>.
- Fabián-Mijangos, A., Min, G. and Alvarez-Quintana, J. (2017), "Enhanced performance thermoelectric module having asymmetrical legs", *Energy Convers. Manage.*, **148**, 1372-1381. <https://doi.org/10.1016/j.enconman.2017.06.087>.
- Lamba, R., Manikandan, S., Kaushik, S. and Tyagi, S. (2018), "Thermodynamic modelling and performance optimization of trapezoidal thermoelectric cooler using genetic algorithm", *Therm. Sci. Eng. Prog.*, **6**, 236-250. <https://doi.org/10.1016/j.tsep.2018.04.010>.
- Lin, S. and Yu, J. (2016), "Optimization of a trapezoid-type two-stage *Peltier* couples for thermoelectric cooling applications", *Int. J. Refriger.*, **65**, 103-110. <https://doi.org/10.1016/j.ijrefrig.2015.12.007>.
- Lv, H., Wang, X.D., Wang, T.H. and Cheng, C.H. (2016), "Improvement of transient supercooling of thermoelectric coolers through variable semiconductor cross-section", *Appl. Energy*, **164**, 501-508. <https://doi.org/10.1016/j.apenergy.2015.11.068>.
- Mallick, M.M., Franke, L., Rösch, A.G. and Lemmer, U. (2020), "Shape-versatile 3d thermoelectric generators by additive manufacturing", *ACS Energy Lett.*, **6**(1), 85-91.

- <https://doi.org/10.1021/acseenergylett.0c02159>.
- Moreno-Navarro, P., Ibrahimbegovic, A. and Pérez-Aparicio, J.L. (2018), “Linear elastic mechanical system interacting with coupled thermo-electro-magnetic fields”, *Couple. Syst. Mech.*, **7**(1), 5-25. <https://doi.org/10.12989/csm.2018.7.1.005>.
- Palma, R., Pérez-Aparicio, J.L. and Bravo, R. (2013), “Study of hysteretic photovoltaic behavior using the finite element method, extended thermodynamic and inverse models”, *Energy Convers. Manage.*, **65**, 557-563.
- Palma, R., Pérez-Aparicio, J.L. and Taylor, R.L.T. (2012), “Non-linear finite element formulation applied to thermoelectric materials under hyperbolic heat conduction model”, *Comput. Meth. Appl. Mech. Eng.*, **213**, 93-103. <https://doi.org/10.1016/j.cma.2011.11.011>.
- Pérez-Aparicio, J.L., Palma, R. and Moreno-Navarro, P. (2016a), “Elasto-thermoelectric non-linear, fully coupled, and dynamic finite element analysis of pulsed thermoelectrics”, *Appl. Therm. Eng.*, **107**, 398-409. <https://doi.org/10.1016/j.applthermaleng.2016.05.114>.
- Pérez-Aparicio, J.L., Palma, R. and Taylor, R.L.T. (2012), “Finite element analysis and material sensitivity of Peltier thermoelectric cells coolers”, *Int. J. Heat Mass Transf.*, **55**, 1363-1374. <https://doi.org/10.1016/j.ijheatmasstransfer.2011.08.031>.
- Pérez-Aparicio, J.L., Palma, R. and Taylor, R.L.T. (2016b), “Multiphysics and thermodynamic formulations for equilibrium and non-equilibrium interactions: Non-linear finite elements applied to multi-coupled active materials”, *Arch. Comput. Meth. Eng.*, **23**(3), 535-583. <https://doi.org/10.1007/s11831-015-9149-9>.
- Rowe, D.M. (2018), *CRC Handbook of Thermoelectrics*, CRC Press.
- Sahin, A.Z. and Yilbas, B.S. (2013), “The thermoelement as thermoelectric power generator: effect of leg geometry on the efficiency and power generation”, *Energy Convers. Manage.*, **65**, 26-32. <https://doi.org/10.1016/j.enconman.2012.07.020>.
- Siddique, A., Venkateshwar, K., Mahmud, S. and Heyst, B.V. (2020), “Performance analysis of bismuth-antimony-telluride-selenium alloy-based trapezoidal-shaped thermoelectric pallet for a cooling application”, *Energy Convers. Manage.*, **222**, 113245. <https://doi.org/10.1016/j.enconman.2020.113245>.
- Taylor, R.L.T. (2010), *FEAP a Finite Element Analysis Program: User Manual*, University of California, Berkeley. <http://www.ce.berkeley.edu/feap>.
- Wang, P., Wang, B., Wang, K., Gao, R. and Xi, L. (2021), “An analytical model for performance prediction and optimization of thermoelectric generators with varied leg cross-sections”, *Int. J. Heat Mass Transf.*, **174**, 121292. <https://doi.org/10.1016/j.ijheatmasstransfer.2021.121292>.

Nomenclature

Symbol	Description	Units
A	Thermoelement cross-section	m^2
l	Thermoelement length	m
κ	Thermal conductivity	W/K
α	Seebeck coefficient	V/K
γ	Electric conductivity	$1/\Omega$
I	Electric current	A
x_i, ξ	Coordinates	m
c_i	Half-width thermoelement	m
ϕ	Form factor	1/m
Q	Heat power	W
V	Electric potential (voltage)	V
T	Temperature	$^{\circ}\text{C}$

n	Number of layers
i	Spatial direction, counter
j	Counter
h	Hot side
c	Cold side
0	Reference
op	Optimal
a, b	Sections: 0, ξ , or l

Abbreviations

TM	Thermoelectric Materials
TE	Thermoelement
FE	Finite Element
TEG	Thermoelectric Generator
TC	Thermocouples
BC	Boundary Condition
VP	Variable Properties
CP	Constant Properties
1D, 2D, 3D	One-, Two-, Three-Dimensional
FEVP	Finite Element code under Variable Properties
FECF	Finite Element code under Constant Properties